CrossMark

TECHNICAL PAPER

Reduction in secondary-actuator displacement in dual-stage actuator system by imparting rotational stiffness in hard disk drives

Shinji Koganezawa · Hirofumi Sano · Hiroshi Tani · Norio Tagawa

Abstract For dual-stage actuator systems in hard disk drives, stroke-saturation of the secondary actuator must be avoided to prevent the servo system from becoming unstable. In this study, a reduction in the secondary-actuator displacement was investigated by imparting a rotational stiffness to a voice coil motor (VCM). It is shown that an increase in the first resonant frequency of the VCM is largely effective for decreasing the secondary-actuator displacement in the general dual-stage actuator system. Then, an actuator, which can impart a rotational stiffness to the VCM, was designed and facilitated. A new control system for dual-stage actuators employing the actuator was also considered. It was confirmed that the proposed servo system reduced the head-positioning errors due to air-flow-induced carriage vibration by more than 35 % compared with a conventional dual-stage actuator system. Furthermore the secondary-actuator displacement was reduced 52 % on average.

1 Introduction

Currently, dual-stage actuator systems based on suspension-level secondary actuators are widely used in hard disk drives (HDDs). The dual-stage actuator servo uses a cooperative control of a voice coil motor (VCM) and secondary actuator and has been applied to achieve head positioning on the order of a few tens of nanometer. The VCM has a wide movable range and is used for relatively coarse actuation. The secondary actuator is utilized for precise positioning especially in the higher frequency range. Because

S. Koganezawa (✉) · H. Sano · H. Tani · N. Tagawa
Kansai University, Suita, Osaka, Japan
e-mail: skoga@kansai-u.ac.jp

the movable range of the secondary actuator is limited and small (e.g., ±0.25–1 μm) (Koganezawa et al. 1998, 2001; Kuwajima et al. 2002; Hirano et al. 2004; Nojima and Koganezawa 2011), stroke saturation of the secondary actuator easily occurs during exposure to a large disturbance. For dual-stage actuators systems, stroke saturation must be prevented to avoid deterioration in the head-positioning accuracy and for stability. An anti-windup controller has been researched to stabilize the dual-stage actuator system to avoid the instability due to stroke saturation (Herrmann et al. 2003). However, this controller causes a decrease in the head-positioning accuracy to some extent. Therefore, minimization of the required secondary-actuator displacement is a fundamental solution to this problem.

2 Reduction in the secondary-actuator displacement

Figure 1 shows an example of the power spectrum of the voltage applied to a secondary actuator when operating in 3.5-inch HDD. Because piezoelectric actuators are used as secondary actuators in this case, the applied voltage is proportional to the secondary actuator displacement. Therefore, a large part of the displacement consists of low-frequency components, as shown in the figure, because the rigid-body-mode vibration induced by the air-flow is the most significant cause of the displacement. Here, a transfer function, y_m/d, of the typical dual-stage actuator system shown in Fig. 2 is given by

$$\frac{y_m}{d} = \frac{C_m P_m P_v}{1 + (1 + KC_m)C_v P_v + C_m P_m} \tag{1}$$

where d is the acceleration disturbance due to the air flow, which is similar to white noise. y_m is the secondary-actuator displacement. P_v and P_m are the plant models of the VCM
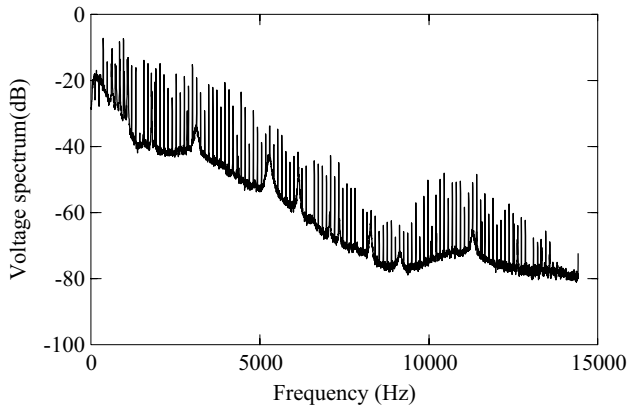
Fig. 1 Power spectrum of the voltage applied to a secondary actuator
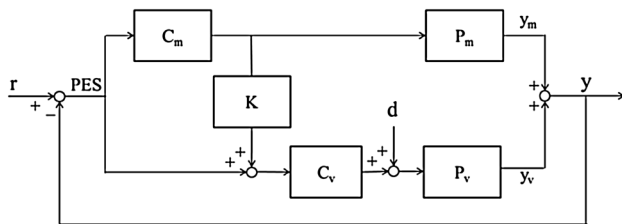
Fig. 2 Block diagram of a dual-stage actuator system

Table 1 VCM plant parameters

i	f_i	ζ_i	A_i
1	90	0.5	1.0
2	3,000	0.01	−0.01
3	4,100	0.03	−1.0
4	5,000	0.01	0.3
5	7,000	0.01	−1.0
6	12,300	0.005	1.0
7	16,400	0.005	−1.0

and secondary actuator, respectively. C_v is a VCM controller, and C_m is a secondary actuator controller. K is the gain for estimating the secondary-actuator displacement. Equation (1) implies that the secondary-actuator displacement can be decreased if we can design the VCM carriage to have a lower compliance. There are generally two measures for attaining a low compliance for P_v: (1) an increase in the moment of inertia of the VCM carriage and (2) an increase in the rotational stiffness that supports the VCM carriage. In either case, these measures cause an increase in the control current or a deterioration in the average seek time. However, the seek performance will not be deteriorated, and the secondary-actuator displacement can be decreased during a tracking operation

Table 2 Secondary actuator plant parameters

f_m	ζ_m	B_m
20,000	0.01	1.0

only if either measure can be selectively activated during a tracking operation.

Assuming that the first resonant-mode frequency f_1 can freely be adjusted by imparting a rotational stiffness, a relationship between f_1 and the required secondary-actuator displacement due to d was calculated as follows.

First, the basic plant models of P_v and P_m were determined referring to "HDD benchmark problem ver. 3" (Yamaguchi et al. 2012), which provides a typical frequency response function (FRF) of the VCM for benchmarking servo controllers. The VCM plant model $P_v(s)$ has seven natural angular frequencies and is given by the following equations:

$$P_v(s) = K_p \sum_{i=1}^{7} \frac{A_i}{s^2 + 2\zeta_i\omega_i s + \omega_i^2} \tag{2}$$

$$\omega_i = 2\pi f_i \tag{3}$$

where K_p is the plant gain and is equal to 3.94×10^9. i is the number of natural modes, A_i is the residue of each mode, and ω_i is the natural angular frequency for mode i. ζ_i is the modal damping ratio. These parameters are listed in Table 1. Then, the secondary actuator was assumed to have a natural frequency of 20 kHz. Its plant model $P_m(s)$ is given by

$$P_m(s) = \frac{B_m \omega_m^2}{s^2 + 2\zeta_m\omega_m s + \omega_m^2} \tag{4}$$

$$\omega_m = 2\pi f_m \tag{5}$$

where B_m is the plant gain, ω_m is the natural angular frequency, and ζ_m is the damping ratio. These parameters are listed in Table 2. Figure 3 shows the FRF of the VCM, P_v, when f_1 varies from 90 to 450 Hz in increments of 120 Hz, and Fig. 4 shows the FRF of the secondary-actuator P_m.

Next, the servo controller was designed as a continuous-time system so that the 0-dB crossover frequency of the open loop for the dual-stage actuator system was 4 kHz. The designed controller of C_v and C_m are as follows:

$$C_v = 3.10 \times 10^{-3} \times \frac{(3s + 1000\pi)(s + 200\pi)}{s(s + 3000\pi)} \times C_N \tag{6}$$

$$C_N = \prod_{j=1}^{5} \frac{s^2 + 2\eta_j\omega_j s + \omega_j^2}{s^2 + 2\xi_j\omega_j s + \omega_j^2} \tag{7}$$
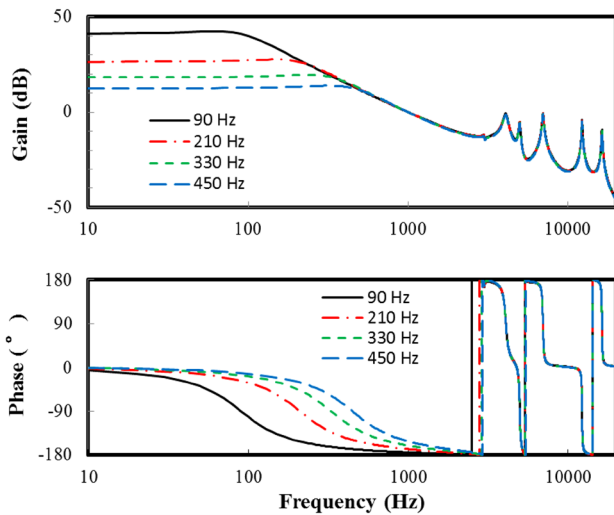
Fig. 3 Transfer function of the VCM plant (P_v) in response to f_1
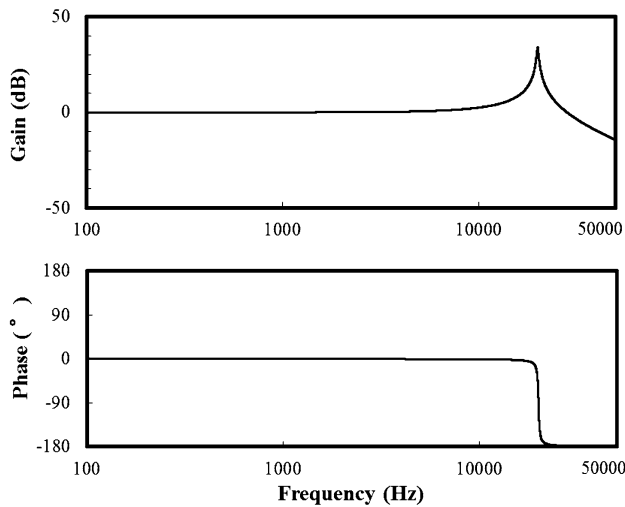

Fig. 4 Transfer function of the secondary actuator plant (P_m)

$$\omega_j = 2\pi f_j \tag{8}$$

$$C_m = 8.20 \times \frac{1000\pi}{s + 1000\pi} \times \frac{s^2 + 800\pi s + (40000\pi)^2}{s^2 + 80000\pi s + (40000\pi)^2} \tag{9}$$

where C_N is a notch filter for the VCM, and its parameters, η_j, ξ_j, and f_j, are listed in Table 3. The open-loop transfer functions in response to f_1 were calculated and are shown in Fig. 5. The gain and phase margins for all cases were 20 dB and 78°, respectively.

Figure 6 shows the transfer functions of y_m/d, and Fig. 7 shows the conclusive results for the secondary-actuator displacement caused by f_1 assuming that d was white noise. As

Table 3 Parameters for the notch filter of the VCM controller

j	f_j	ξ_j	η_j
1	4,100	0.25	0.025
2	5,000	0.15	0.015
3	7,000	0.4	0.012
4	12,300	0.4	0.004
5	16,400	0.45	0.0045

the basic value of f_1 was 90 Hz, the required displacement was normalized by the displacement in the case where f_1 was 90 Hz. It can be seen that an increase in f_1 decreases the secondary-actuator displacement. When f_1 is 400 Hz, the required displacement decreases to approximately half its basic value. On the other hand, the compliance of the VCM carriage decreases with the increase in f_1, and the required current must increase.

Figure 8 shows the relationship between f_1 and the stiffness at 120 Hz. The stiffness at 120 Hz is proportional to the VCM current for compensating the major repeatable run-out (RRO) component of 120 Hz when disks rotate at 7,200 rpm. Thus, an increase in the stiffness at 120 Hz roughly indicates an increase in the required current. When f_1 increases to 400 Hz, the required current is approximately 10 times that at 90 Hz, although the power consumption for tracking is very small compared with seek operations. Thus, there is a trade-off between the secondary-actuator displacement and the VCM current. An adequate value for f_1 should be determined considering this trade-off relationship.

In this study, an actuator, which can impart a rotational stiffness to the VCM carriage on demand, was investigated. The mechanism and characteristics of the actuator are discussed in this paper. In addition, we considered the possibility of a new control scheme for dual-stage actuators employing the actuator during a tracking operation. Although the actuator design is unsophisticated, it is functional enough to study the feasibility of the imparting-on-demand mechanism.

3 Electromagnetic actuator

In this section, the developed actuator that can impart a rotational stiffness will be described. Figure 9 shows a schematic of the developed electromagnetic actuator. The stator of the actuator consists of a stator yoke, which is the fixed part on the HDD base; a magnetic-material bobbin; and a coil, which is wound around the bobbin. A cross-shaped flat spring, whose outer circular area is fixed to the stator yoke and whose inner area is fixed to the moving shaft, connects the moving part and stator. The moving part consists of a
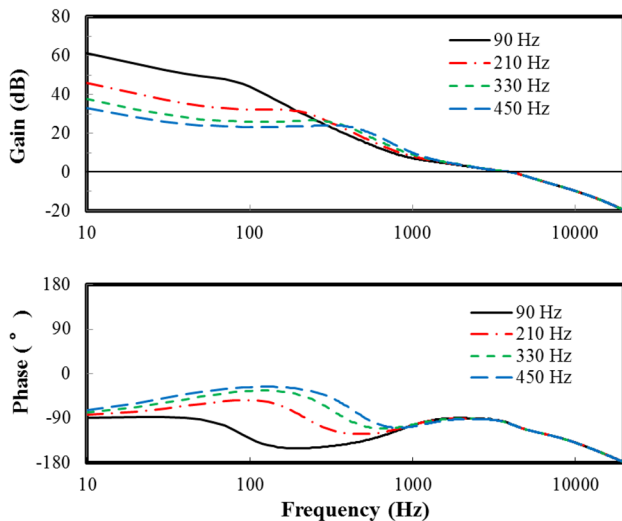
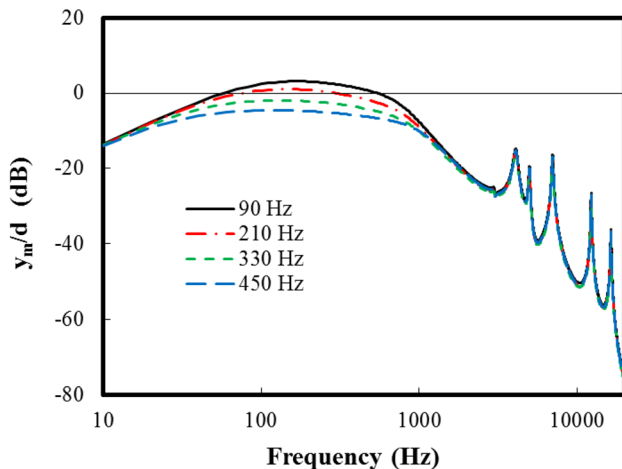Fig. 5 Open-loop transfer function of the dual-stage actuator system in response to f_1

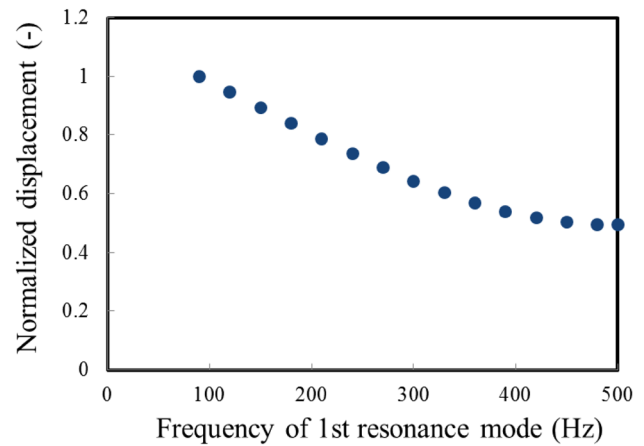Fig. 6 Transfer functions of y_m/d in response to f_1

Fig. 7 Secondary-actuator displacement in response to the first resonant frequency
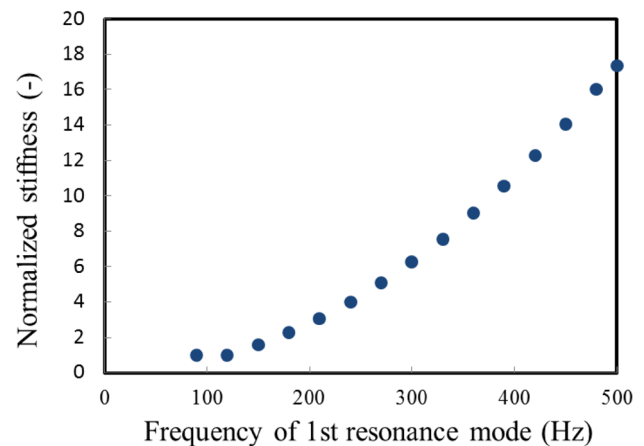
Fig. 8 Stiffness of the VCM at 120 Hz in response to the first resonant frequency

moving shaft and magnetic-material moving plate. There is a small gap of approximately 100 µm between the stator yoke and the moving plate. When current is applied to the coil, a magnetic flux is generated in the bobbin, and magnetic attraction occurs between the stator yoke and the moving plate. Thus, the moving part moves upward.

Figure 10 shows the prototype actuator, and Fig. 11 shows a photograph of the actuator in use with a VCM carriage. The electromagnetic actuator was placed between the HDD base and the VCM carriage. During seek operations, the actuator is suspended, and the VCM can rotate freely as in normal HDDs. During tracking operations, the actuator is activated, and the top surface of the moving shaft of the actuator comes into contact with the VCM carriage. A friction force acts between the VCM carriage and the moving shaft, and the VCM becomes supported by the actuator structure,

thereby imparting a rotational stiffness to the VCM, which is determined by the stiffness in the in-plane direction of the flat spring. When the current is no longer supplied to the coil, the moving plate returns to its original position by the spring force of the flat spring, and the carriage is free to rotate.

The design specifications of the actuator are listed in Table 4. The height of the prototype actuator is 4 mm, and the outer diameter is 15 mm. Because the prototype actuator is all hand-made, its size is too large, and a downsized design is necessary for application to multiple-platter HDDs. The supply voltage is 5 V, and the generation force should be >30 mN. The flat spring was made of a phosphor copper bronze sheet (C5191P-H). The stiffness of the flat spring in the out-of-plane direction is related to its operating time, and the stiffness in the in-plane direction is related to the rotational stiffness imparted to the VCM. The magnetic material of the yoke and bobbin was carbon steel (S15C), and the moving shaft was made of aluminum.

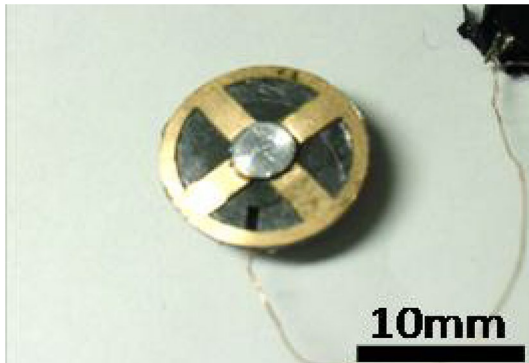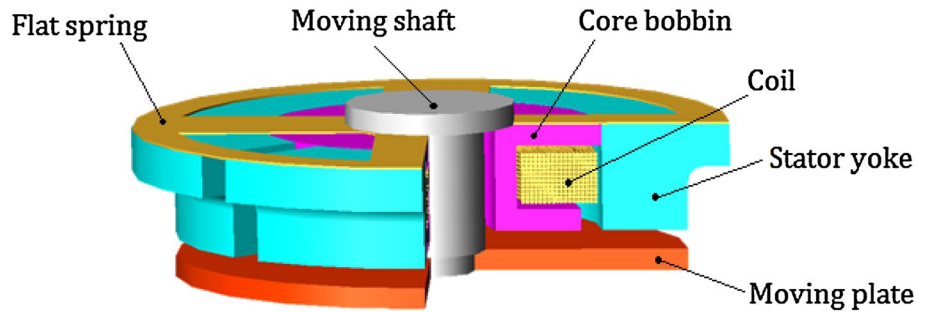**Fig. 9** Schematic of the developed electromagnetic actuator

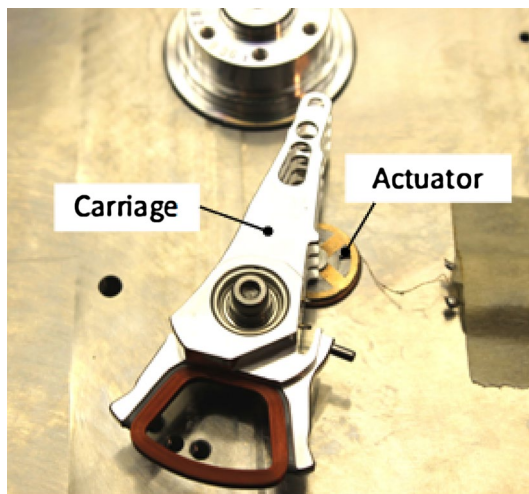**Fig. 10** Photograph of the prototype electromagnetic actuator

Fig. 11 Photograph of the VCM carriage and developed electromagnetic actuator

Table 4 Design specifications for the electromagnetic actuator

Specifications	Value
Voltage	5 V
Gap thickness between stator yoke and moving plate	100 μm
Required contact force	>30 mN
Operating time	<1 ms
Dimension	
Total height	4 mm
Diameter	15 mm
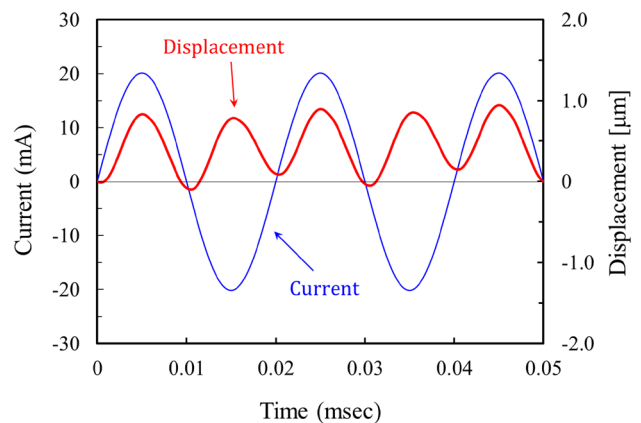
Fig. 12 Displacement of the moving shaft when a 50-Hz sinusoidal current is applied

4 Evaluation of the prototype actuator

Figure 12 shows the displacement of the moving shaft when a 50 Hz sinusoidal current is applied to the coil. Regardless of the current direction, a magnetic attractive force activates the same direction, and the displacement of the moving shaft is always upward. Because the attractive force is a function of the square of the applied current, the

frequency of the displacement becomes twice the frequency of the current. Figure 13 shows the maximum contact force generated by the magnetic attractive force in response to an applied current. The maximum force, by which the moving plate was detached from the stator yoke when a current was applied, was measured by a load cell. The filled circles indicate the force measured with a load cell, and the solid line indicates the theoretical curve calculated by the following equation:

$$F = K(z)\frac{(NI)^2}{2\mu_0} - kz \tag{10}$$

where N is the number of turns of the coil and is 252, and μ_0 is the absolute permeability in vacuum. $K(z)$ is a
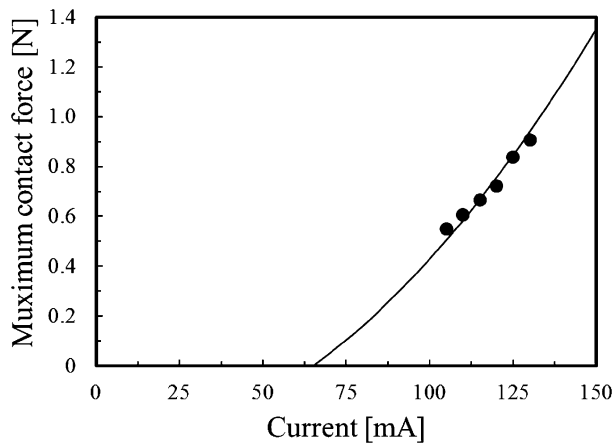
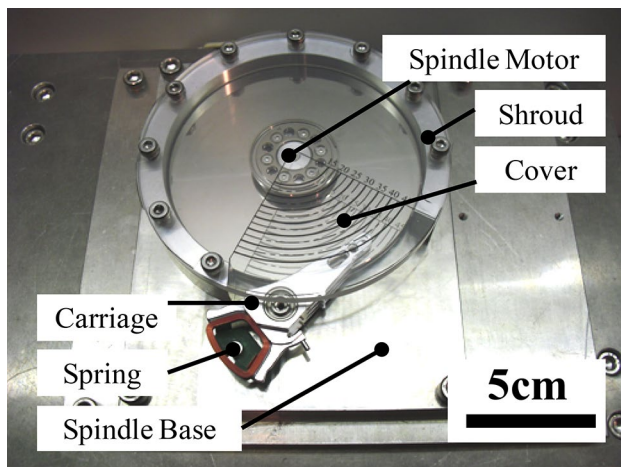**Fig. 13** Contact force generated by the actuator

**Fig. 14** HDD-like tool for air-flow-induced vibration of the carriage arm

coefficient, which depends on a permeance coefficient, and is a function of the gap thickness z. k is the stiffness in the out-of-plane direction of the flat spring and is 5,000 N/m. According to Fig. 13, the actuator generates a large enough contact force. The measured gap thickness between the stator yoke and the moving plate was 62.4 μm. The operation time of the actuator was 0.9 ms at 145 mA, which satisfied the design specifications.

### 4.1 Actuator evaluation using an HDD-like tool

Figure 14 shows the HDD-like tool for actuator evaluation that consists of a spindle motor, which rotates 7,200 rpm; a VCM carriage; a 270° shroud; a clear cover; and the developed actuator. Two disks with a diameter of 95 mm and a thickness of 1.27 mm were stacked on the spindle motor. The 270° shroud surrounded the disks. The actuator was placed between the base and the VCM carriage to impart
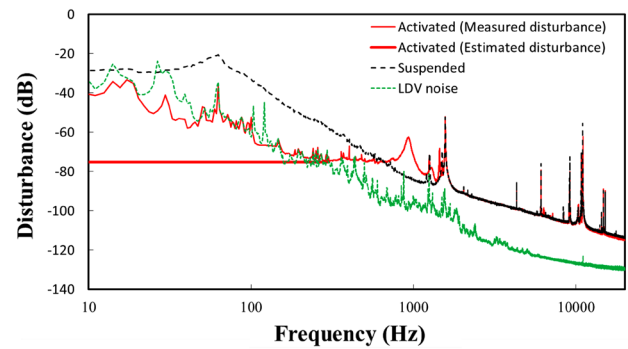
(a) Outer track of the disk (r = 42.5 mm)
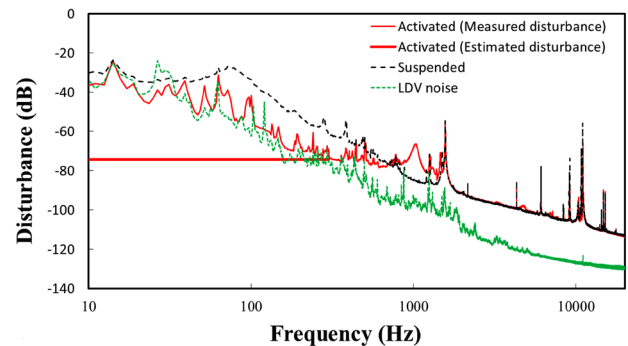
(b) Center track of the disk (r = 32.5 mm)
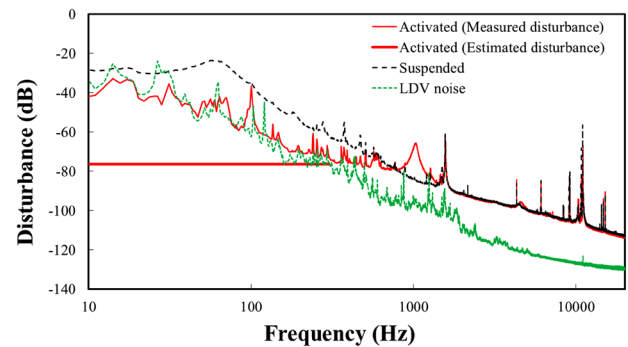
(c) Inner track of the disk (r = 25 mm)

Fig. 15 Power spectra of carriage vibration

a rotational stiffness to the carriage. The contact point of the moving shaft is 17 mm from the rotational axis of the VCM. The measured clearance between the carriage arm and the moving shaft was approximately 50 μm.

The air-flow-induced carriage vibration of the carriage-arm tip between the two disks was measured with a laser Doppler vibrometer (LDV). The VCM carriage was always supported by another spring, which has a low rotational stiffness to keep the carriage from moving for stable laser reflection during LVD measurement.

Figure 15 shows the power spectra of the carriage-arm-tip vibration induced by the air-flow with the

developed actuator suspended and activated. When the actuator is suspended, the carriage vibration is large, and a resonance appears at 60 Hz. This resonant frequency is determined by the spring for LDV measurement and the moment of inertia of the VCM carriage. When the actuator is activated with an electrical current of 0.15 A, a resonance appears at 930 Hz, and the spectrum gain is flat below the resonant frequency. This is because a rotational stiffness was imparted by the contact between the VCM carriage and the moving shaft. The contact force was estimated at 1.24 N from Eq. (10). According to these results, air-flow-induced carriage vibration was largely suppressed by imparting a rotational stiffness effectively. However, a lower rotational stiffness should be better for the general dual-stage servo as mentioned in Sect. 2 from a power-consumption perspective, which can be achieved by a narrower design for the flat spring. Note that the measurement noise of the LDV was observed to be less than 300 Hz. Considering that the acceleration disturbance due to the air-flow is similar to white noise, the vibration spectrum without LDV noise was estimated to be the average of the values between 300 and 500 Hz. The estimated vibration spectra are indicated by the bold line in Fig. 15. For the suspended case, however, the LDV noise was ignored because it only had an effect at frequencies less than 50 Hz, and its effects on the NRPE and secondary-actuator displacement were small. This is because the gains of the sensitivity function and y_m/d were low enough at frequencies less than 50 Hz.

4.2 Consideration of the feasibility of a new servo system

In the previous section, the carriage-vibration spectra when the actuator was activated and suspended were determined. It was observed that the VCM vibration was sufficiently suppressed by activating the developed actuator. Therefore, the VCM controller gain for a general dual-stage actuator system does not need to be high in this case. Then, we considered the feasibility of a new control system for dual-stage actuators with the developed actuator. In the new servo system, a secondary-actuator servo (SAS), the VCM follows only the RRO using feed-forward control, and the secondary actuator follows the other component in which non-repeatable run-out (NRRO) is mainly included. The secondary actuator was the same as that in Fig. 4. The block diagram of the SAS is shown in Fig. 16. The controller for the SAS was also designed as a continuous-time system so that the 0-dB crossover frequency of the open loop was set to 4 kHz. The designed controller for SAS is as follows:

$$C_{SAS} = 20.8 \times \frac{400\pi}{s + 400\pi} \times \frac{s^2 + 800\pi s + (40000\pi)^2}{s^2 + 80000\pi s + (40000\pi)^2}$$
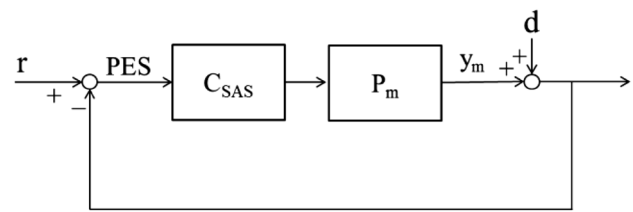
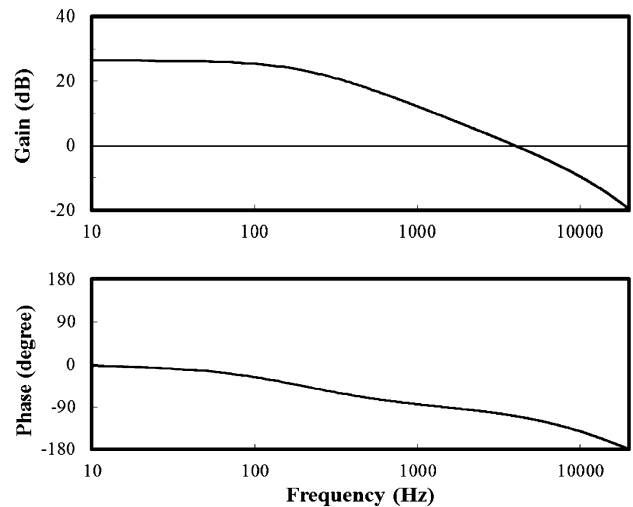(11)

Fig. 16 Block diagram of the SAS

Fig. 17 Open-loop transfer function of the SAS
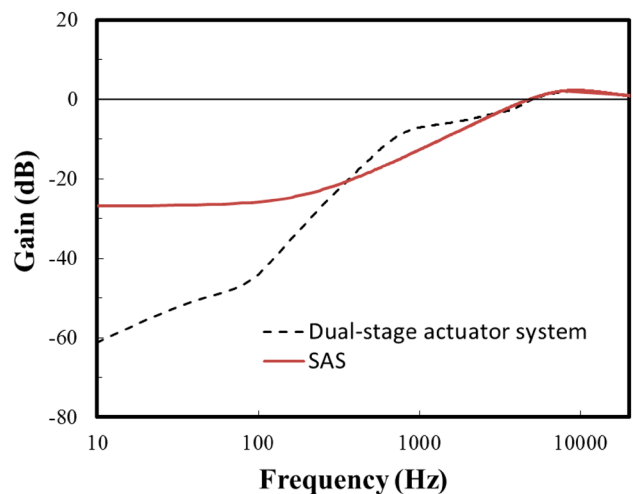

Fig. 18 Sensitivity function comparison of the dual-stage actuator system and SAS

Figures 17 and 18 show the open-loop transfer function and sensitivity function, respectively. The gain and phase margins of the SAS were 19.8 dB and 70°, respectively. From the transfer functions and power spectra of the VCM vibration at outer, center, and inner tracks, the position
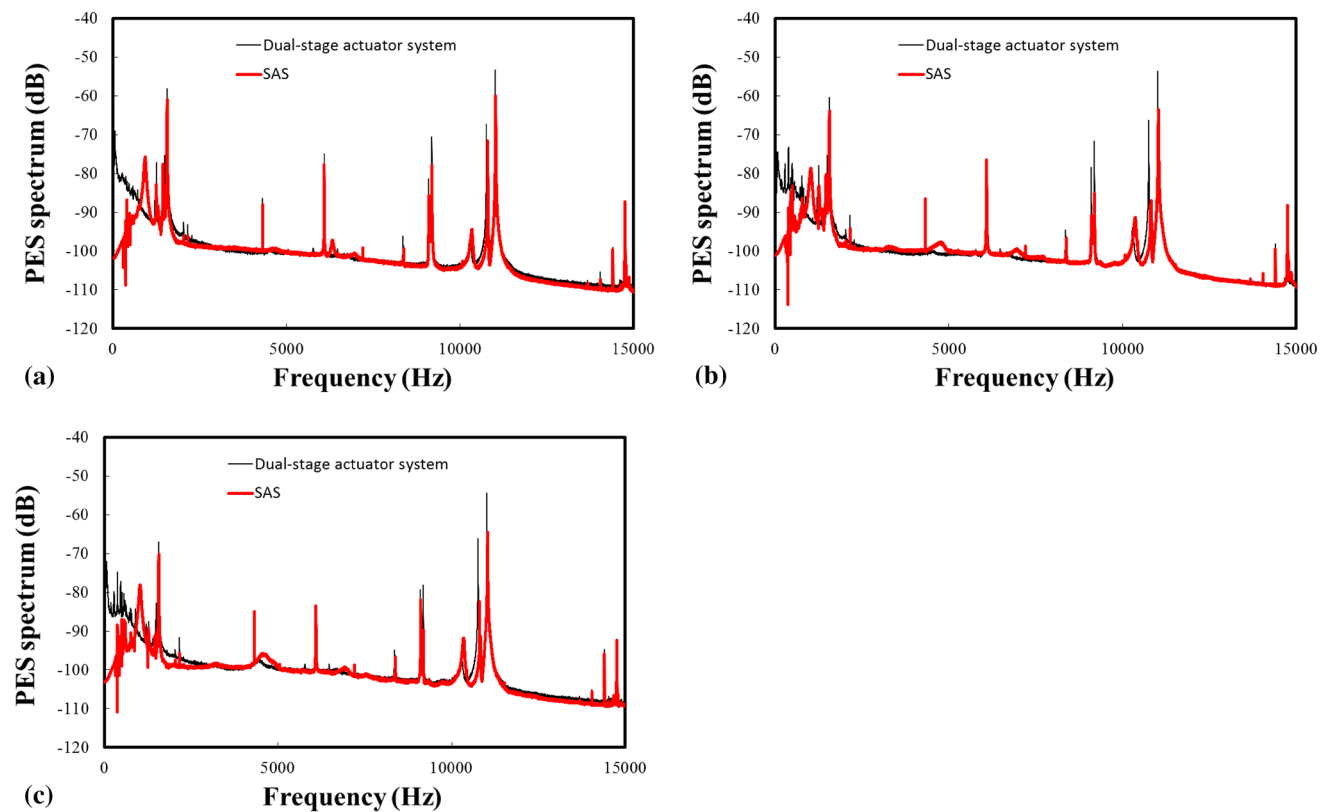
Fig. 19 Power spectra of the NRPE

Table 5 3σ of the NRPE (nm)

	SAS	Dual-stage actuator	Reduction ratio (%)
Outer	9.01	13.91	35.2
Center	7.80	13.16	40.7
Inner	6.52	11.20	41.8

error and secondary-actuator displacement due to *d* were calculated.

Figure 19 shows the power spectra of the position errors of the dual-stage actuator system and SAS. The SAS largely suppressed disturbances at frequencies less than 1 kHz compared with the dual-stage actuator system. Table 5 lists three times the standard deviation (3σ) of the non-repeatable position error (NRPE). The NRPE of the SAS was reduced by 35 to 42 %.

Figure 20 shows the spectra of the secondary-actuator displacement. The displacement of the SAS is greatly reduced in the frequency range less than 1.3 kHz. Table 6 lists 3σ of the secondary-actuator displacement. The displacement of the SAS was reduced by 52 % on average. Therefore, the SAS can not only improve the head-positioning error but also reduce the secondary-actuator

displacement. The drawback of the SAS is that the electric current for compensating the 120-Hz RRO component becomes 60 times greater than that for typical VCM servos in this case.

5 Conclusion

In this study, a reduction in the secondary-actuator displacement was investigated by imparting a rotational stiffness to the VCM carriage. It was clearly demonstrated that an increase in the first resonant frequency of the VCM greatly decreases the secondary-actuator displacement. On the other hand, the compliance of the VCM decreases with an increase in the resonant frequency, and the required current must increase.

An electromagnetic actuator, which can impart a rotational stiffness to the VCM, was designed and fabricated. The actuator generated a force >30 mN and was able to impart a rotational stiffness to the VCM effectively.

We also considered a new control system, called the SAS, for dual-stage actuators that employed an additional electromagnetic actuator. It was confirmed that the SAS reduced the head-positioning errors due to
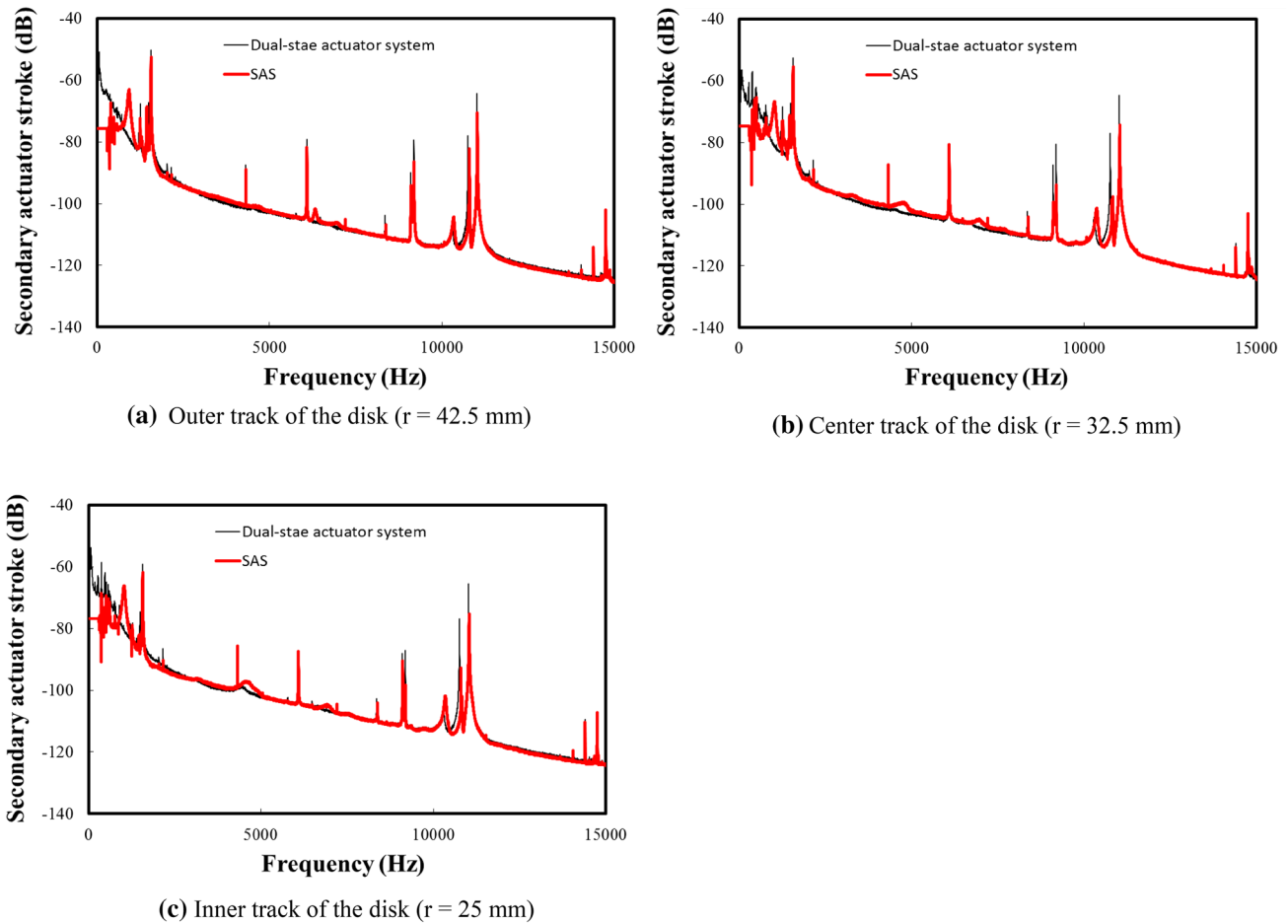
(a) Outer track of the disk (r = 42.5 mm)

(b) Center track of the disk (r = 32.5 mm)

(c) Inner track of the disk (r = 25 mm)

Fig. 20 Power spectra of the secondary-actuator displacement

Table 6 3σ of the secondary-actuator displacement (nm)

	SAS	Dual-stage actuator	Reduction ratio (%)
Outer	24.0	49.2	51.2
Center	20.5	39.5	48.1
Inner	16.5	38.0	56.6

air-flow-induced carriage vibration by more than 35 % compared with a conventional dual-stage actuator system. Furthermore, the secondary-actuator stroke was reduced by 52 % on average.

References

Herrmann G, Turner MC, Postlethwaite I, Guo G (2003) Application of a novel anti-windup scheme to a HDD-dual-stage actuator. Proc Am Control Conf 1:743–748

Hirano T, White M, Yang H, Scott K, Pattanaik S, Arya S, Huang F (2004) A moving-slider MEMS actuator for high-bandwidth HDD tracking. IEEE Trans Magn 40(4):3171–3173

Koganezawa S, Uematsu Y, Yamada T (1998) Shear mode piezoelectric microactuator for magnetic disk drives. IEEE Trans Magn 34(4):1910–1912

Koganezawa S, Hara T, Uematsu Y, Yamada T (2001) Effect of dual-stage actuator on positioning accuracy in 10 k rpm magnetic disk drives. IEEE Trans Magn 37(2):955–958

Kuwajima H, Uchiyama H, Ogawa Y, Kita H, Matsuoka K (2002) Manufacturing process of piezoelectric thin-film dual-stage actuator and its reliability for HDD. IEEE Trans Magn 38(5):2156–2158

Nojima Y, Koganezawa S (2011) Newly designed slider-based microactuator for magnetic disk drive. J Adv Mech Des Syst Manuf 5(1):45–53

Yamaguchi T, Hirata M, Pang CK (2012) High-speed precision motion control. CRC Press, ISBN: 978-1-4398-6726-6